ÓPTICA PURA Y APLICADA
www.sedoptica.es

Type: REVIEW PAPER
Section: Imaging Techniques

Optical Codification Design in Compressive Spectral Imaging: From Mathematical to Deep Learning Optimization

Laura Galvis and Henry Arguello*

Department of Computer Science, Universidad Industrial de Santander, Bucaramanga, 680002, Colombia

(*)E-mail: henarfu@uis.edu.co S: miembro de SEDOPTICA / SEDOPTICA member

Received: 01/12/2021 Accepted: 11/02/2022
DOI: 10.7149/OPA.55.1.51083

ABSTRACT:

The optical codification in compressive spectral imaging has been an area of continuous improvement. The study of the coded apertures as modulation devices and their contribution to the final spectral image quality have allowed proposing different methods of coded aperture optimization. Four different coded aperture design approaches developed through the years are reported to show the improvement process, followed by the comparison of the resulting designs in the reconstruction of spectral images. Furthermore, the latest research on deep learning-based methods has resulted in additional tools for the designs, opening more opportunities in this area of research.

Key words: Compressive Imaging; Optical Codification; Compressive Sensing; Spectral Imaging, deep learning.

REFERENCES AND LINKS / REFERENCIAS Y ENLACES

[1] D. Wu and D.-W. Sun, "Advanced applications of hyperspectral imaging technology for food quality and safety analysis and assessment: A review—Part I: Fundamentals," Innovative Food Science & Emerging Technologies **19**, 1–14 (2013).

[2] Y. Liu, H. Pu, and D.-W. Sun, "Hyperspectral imaging technique for evaluating food quality and safety during various processes: A review of recent applications," Trends in Food Science Technology **69**, 25–35 (2017).

[3] Q. Li, X. He, Y. Wang, H. Liu, D. Xu, and F. Guo, "Review of spectral imaging technology in biomedical engineering: achievements and challenges," Journal of biomedical optics **18**(10), 100,901–100,901 (2013).

[4] B. Fei, "Chapter 3.6 - Hyperspectral imaging in medical applications," in Hyperspectral Imaging, J. M. Amigo, ed., vol. 32 of Data Handling in Science and Technology, pp. 523–565 (Elsevier, 2020).

[5] M. T. Eismann, "Hyperspectral remote sensing," (SPIE Bellingham, 2012).

[6] Y. Gu, T. Liu, G. Gao, G. Ren, Y. Ma, J. Chanussot, and X. Jia, "Multimodal hyperspectral remote sensing: an overview and perspective," Science China Information Sciences **64**(2), 121,301 (2021).

[7] M. Shimoni, R. Haelterman, and C. Perneel, "Hypersectral Imaging for Military and Security Applications: Combining Myriad Processing and Sensing Techniques," IEEE Geoscience and Remote Sensing Magazine **7**(2), 101–117 (2019).

[8] A. Stern, "Optical Compressive Imaging," (2016).

[9] D. Donoho, "Compressed sensing," IEEE Transactions on Information Theory **52**(4), 1289–1306 (2006).

[10] E. Candes, J. Romberg, and T. Tao, "Robust uncertainty principles: exact signal reconstruction from highly incomplete frequency information," IEEE Transactions on Information Theory **52**(2), 489–509 (2006).

[11] C. Li, T. Sun, K. F. Kelly, and Y. Zhang, "A Compressive Sensing and Unmixing Scheme for Hyperspectral Data Processing," IEEE Transactions on Image Processing **21**(3), 1200–1210 (2012).

[12] X. Yuan, T.-H. Tsai, R. Zhu, P. Llull, D. Brady, and L. Carin, "Compressive Hyperspectral Imaging With Side Information," IEEE Journal of Selected Topics in Signal Processing **9**(6), 964–976 (2015).

[13] G. R. Arce, D. J. Brady, L. Carin, H. Arguello, and D. S. Kittle, "Compressive Coded Aperture Spectral Imaging: An Introduction," IEEE Signal Processing Magazine **31**(1), 105–115 (2014).

[14] J. M. Ramirez, J. I. Martínez Torre, and H. Arguello, "Feature fusion via dual-resolution compressive measurement matrix analysis for spectral image classification," Signal Processing: Image Communication **90**, 116,014 (2021).

[15] J. M. Bioucas-Dias and M. A. T. Figueiredo, "A New TwIST: Two-Step Iterative Shrinkage/Thresholding Algorithms for Image Restoration," IEEE Transactions on Image Processing **16**(12), 2992–3004 (2007).

[16] M. Figueiredo, R. D. Nowak, and S. J. Wright, "Gradient Projection for Sparse Reconstruction: Application to Compressed Sensing and Other Inverse Problems," Selected Topics in Signal Processing, IEEE Journal of **1**(4), 586–597 (2007).

[17] A. Rajwade, D. Kittle, T.-H. Tsai, D. Brady, and L. Carin, "Coded Hyperspectral Imaging and Blind Compressive Sensing," SIAM Journal on Imaging Sciences **6**(2), 782–812 (2013).

[18] J. Tan, Y. Ma, H. Rueda, D. Baron, and G. R. Arce, "Compressive Hyperspectral Imaging via Approximate Message Passing," IEEE Journal of Selected Topics in Signal Processing **10**(2), 389–401 (2016).

[19] L. Wang, C. Sun, Y. Fu, M. H. Kim, and H. Huang, "Hyperspectral Image Reconstruction Using a Deep Spatial-Spectral Prior," in 2019 IEEE/CVF Conference on Computer Vision and Pattern Recognition (CVPR), pp. 8024–8033 (2019).

[20] L. Wang, T. Zhang, Y. Fu, and H. Huang, "HyperReconNet: Joint Coded Aperture Optimization and Image Reconstruction for Compressive Hyperspectral Imaging," IEEE Transactions on Image Processing **28**(5), 2257–2270 (2019).

[21] H. Arguello, S. Pinilla, Y. Peng, H. Ikoma, J. Bacca, and G. Wetzstein, "Shift-variant color-coded diffractive spectral imaging system," Optica **8**(11), 1424–1434 (2021).

[22] H. Arguello and G. R. Arce, "Colored Coded Aperture Design by Concentration of Measure in Compressive Spectral Imaging," IEEE Transactions on Image Processing **23**(4), 1896–1908 (2014).

[23] L. Galvis, H. Arguello, and G. R. Arce, "Coded aperture design in mismatched compressive spectral imaging," Appl. Opt. **54**(33), 9875–9882 (2015).

[24] C. V. Correa, H. Arguello, and G. R. Arce, "Spatiotemporal blue noise coded aperture design for multi-shot compressive spectral imaging," J. Opt. Soc. Am. A **33**(12), 2312–2322 (2016).

[25] L. Galvis, D. Lau, X. Ma, H. Arguello, and G. R. Arce, "Coded aperture design in compressive spectral imaging based on side information," Appl. Opt. **56**(22), 6332–6340 (2017).

[26] Y. Mejia and H. Arguello, "Binary Codification Design for Compressive Imaging by Uniform Sensing," IEEE Transactions on Image Processing **27**(12), 5775–5786 (2018).

[27] L. Galvis, E. Mojica, H. Arguello, and G. R. Arce, "Shifting colored coded aperture design for spectral imaging," Appl. Opt. **58**(7), B28–B38 (2019).

[28] H. Garcia, C. V. Correa, and H. Arguello, "Optimized Sensing Matrix for Single Pixel Multi-Resolution Compressive Spectral Imaging," IEEE Transactions on Image Processing **29**, 4243–4253 (2020).

[29] E. Mojica, C. V. Correa, and H. Arguello, "High-resolution coded aperture optimization for super-resolved compressive x-ray cone-beam computed tomography," Appl. Opt. **60**(4), 959–970 (2021).

[30] J. Bacca, T. Gelvez, and H. Arguello, "Deep Coded Aperture Design: An End-to-End Approach for Computational Imaging Tasks," (2021). 2105.03390.

[31] J. Bacca, L. Galvis, and H. Arguello, "Coupled deep learning coded aperture design for compressive image classification," Opt. Express **28**(6), 8528–8540 (2020).

[32] C. Hinojosa, J. Bacca, and H. Arguello, "Coded Aperture Design for Compressive Spectral Subspace Clustering," IEEE Journal of Selected Topics in Signal Processing **12**(6), 1589–1600 (2018).

[33] K. M. León-López, L. V. Galvis Carreño, and H. Arguello Fuentes, "Temporal Colored Coded Aperture Design in Compressive Spectral Video Sensing," IEEE Transactions on Image Processing **28**(1), 253–264 (2019).

[34] R. Jacome, J. Bacca, and H. Arguello, "Deep-Fusion: An End-To-End Approach for Compressive Spectral Image Fusion," in 2021 IEEE International Conference on Image Processing (ICIP), pp. 2903–2907 (2021).

[35] X. Cao, T. Yue, X. Lin, S. C.-F. Lin, X. Yuan, Q. Dai, L. Carin, and D. J. Brady, "Computational Snapshot Multispectral Cameras: Toward dynamic capture of the spectral world," IEEE Signal Processing Magazine **33**, 95–108 (2016).

[36] J. Chang and G. Wetzstein, "Deep Optics for Monocular Depth Estimation and 3D Object Detection," in

Proceedings of the IEEE International Conference on Computer Vision (2019).

[37] A. Wagadarikar, R. John, R. Willett, and D. Brady, "Single disperser design for coded aperture snapshot spectral imaging," Appl. Opt. **47**(10), B44–B51 (2008).

[38] T.-H. Tsai and D. J. Brady, "Coded aperture snapshot spectral polarization imaging," Appl. Opt. **52**(10), 2153–2161 (2013).

[39] X.-J. Lai, H.-Y. Tu, Y.-C. Lin, and C.-J. Cheng, "Coded aperture structured illumination digital holographic microscopy for superresolution imaging," Opt. Lett. **43**(5), 1143–1146 (2018).

[40] S. Pinilla, J. Poveda, and H. Arguello, "Coded diffraction system in X-ray crystallography using a boolean phase coded aperture approximation," Optics Communications **410**, 707–716 (2018).

[41] Y. Qiao, N. Jing, R. Zhang, Z. Wang, and J. Li, "Intensity modulation-based spectral polarization measurement method of coded aperture," Optics Communications **437**, 128–132 (2019).

[42] J. M. Ramirez, J. I. Martínez-Torre, and H. Arguello, "LADMM-Net: An unrolled deep network for spectral image fusion from compressive data," Signal Processing **189**, 108,239 (2021).

[43] M. E. Gehm, R. John, D. J. Brady, R. M. Willett, and T. J. Schulz, "Single-shot compressive spectral imaging with a dual-disperser architecture," Opt. Express **15**(21), 14,013–14,027 (2007).

[44] X. Lin, G. Wetzstein, Y. Liu, and Q. Dai, "Dual-coded compressive hyperspectral imaging," Opt. Lett. **39**(7), 2044–2047 (2014).

[45] M. Marquez, P. Meza, H. Arguello, and E. Vera, "Compressive spectral imaging via deformable mirror and colored-mosaic detector," Opt. Express **27**(13), 17,795–17,808 (2019).

[46] R. D. Richard Baraniuk, Mark Davenport and M. Wakin, "A Simple Proof of the Restricted Isometry Property for Random Matrices," Constructive Approximation **28**(6), 253–263 (2008).

[47] J. Bacca, T. Gelvez, and H. Arguello, "Transmittance Regularizer for Binary coded Aperture Design in a Computational Imaging end-to-end Approach," in ICASSP 2021 - 2021 IEEE International Conference on Acoustics, Speech and Signal Processing (ICASSP), pp. 1470–1474 (2021).

[48] E. Vargas, J. N. P. Martel, G. Wetzstein, and H. Arguello, "Time-Multiplexed Coded Aperture Imaging: Learned Coded Aperture and Pixel Exposures for Compressive Imaging Systems," in Proceedings of the IEEE/CVF International Conference on Computer Vision (ICCV), pp. 2692–2702 (2021).

[49] E. J. Candes and M. B. Wakin, "An Introduction To Compressive Sampling," IEEE Signal Processing Magazine **25**(2), 21–30 (2008).

[50] Y. Zhao, W. He, Z. Liu, and Y. Fu, "Optical design of an Offner coded aperture snapshot spectral imaging system based on dual-DMDs in the mid-wave infrared band," Opt. Express **29**(24), 39,271–39,283 (2021).

[51] F. J. Herrmann, M. P. Friedlander, and Ö. Yilmaz, "Fighting the curse of dimensionality: Compressive sensing in exploration seismology," IEEE Signal Processing Magazine **29**(3), 88–100 (2012).

[52] L. Galvis, J. M. Ramírez, E. Vargas, O. Villarreal, W. Agudelo, and H. Arguello, "Reconstruction of 2D seismic wavefields from nonuniformly sampled sources," IS and T International Symposium on Electronic Imaging Science and Technology **2020**(6) (2020).

[53] S. Pinilla, H. García, L. Díaz, J. Poveda, and H. Arguello, "Coded aperture design for solving the phase retrieval problem in X-ray crystallography," Journal of Computational and Applied Mathematics **338**, 111–128 (2018).

1. Introduction

The computational imaging area has extended its capabilities and applications since compressive sensing (CS) emerged. CS as a sensing paradigm has been exploited in this area by using coded apertures based on the important assumption that the design of an efficient sensing protocol and posterior use of computational power will produce high fidelity reconstruction of the high dimensional information; this scheme is usually termed as coded-aperture imaging. An example of high dimensional information is the spectral images (SI), which can be described as images with spatial information across a large number of wavelengths. The amount of sensed data when dealing with SI increases with the number of bands. Therefore, the size of the SI is not only an issue in the acquisition but also the storage, and processing of the information. Many applications using hyperspectral imaging (HSI) have conveniently used CS aiming for the reduction of sensed data. For instance, quality control in food and industrial agriculture [1, 2], medical imaging [3, 4], remote sensing [5, 6], security applications [7], among others [8].

Inspired by the advantages of CS [9, 10], researchers, mainly those from the optical imaging area, have adopted this joint sensing and reconstruction scheme known as compressive spectral imaging (CSI) that sense a three-dimensional (3D) data cube through just a few two-dimensional (2D) measurements [11, 12]. Then, the underlying high dimensional scene is recovered using CS inversion algorithms. CSI has gained popularity since CSI systems require fewer measurements than those attained with traditional hyperspectral imaging sensors [13, 14]. Consequently, the complexity of these systems relies upon computational algorithmic development and postprocessing.

CSI relies on two principles, the sparsity of the signal or its representation in a domain where the signal expresses its sparse properties [12]. The second principle, incoherence sampling, refers to the way scenes are acquired in their original domain, which can be found through the analysis of the sensing matrix, since it relates the sampling matrix, which describes the transfer function of the system and the representation basis where the signal is sparse.

The reconstruction is accomplished using optimization algorithms to solve the resulting ill-conditional linear system of equations [15–18]. The basis of these numerical algorithms is to solve the inverse compressive sensing problem, minimizing the error with respect to the compressed measurements by means of the ℓ_2 norm, and penalizing the objective function by the ℓ_1 norm, forcing the solution to be sparse. New algorithms and approaches, including for instance *a priori* information in the form of additional regularizers, are continuously proposed. Lastly, with the trend of deep learning, learning-based algorithms have also been reported in the literature [19, 20].

1.1. Motivation

The active research on CSI has enabled the development of novel cameras. However, their development has shown many challenges and, therefore, future research directions:

- Although CSI has shown advantages in reducing sensed data, the complexity reduction of the optical implementations of those architectures is still open. The challenge is to produce more flexible and portable systems. Regarding the codification in the implementation of coded-aperture imaging, new coding devices are under study, opening opportunities to develop new optical architectures [21].
- Recent works have focused on designing the coded aperture (CA) patterns to improve the accuracy of the reconstructions of high-dimensional images [22–30]. In addition to the reconstruction, they also report the effect of the designed codes in the subsequent high-level applications such as classification [31], clustering [32], spectral video [33], fusion [34], etc. The advent of deep learning in coded aperture optimization opens even more, the broad space for improvements and applications.

This work provides an overview focused on the coded aperture design approaches to acquire compressive spectral images. The methods have been the result of constant improvements and a deeper understanding of the CA operation. Specifically, the methods reported have been produced by a Colombian research group, the High Dimensional Research Group - HDSP, from the Universidad Industrial de Santander [22–30, 32–34]. The CA designs are divided into four categories: geometrical optimization, l_2 mathematical optimization, restricted isometry property (RIP) mathematical optimization, and data-based. In each of the categories, some works have led to demonstrate the capabilities of each of the approaches.

The remainder of this paper is organized as follows. Section 2 describes the codification in compressive spectral imaging, specifically the role of the coded aperture in the forward model and the reconstruction of the spectral images. Section 3 presents a detailed analysis of the different coded aperture design methods. Section 4 reports new coded aperture design improvements achieved using deep learning methods, and the review ends with concluding remarks in Sec. 6.

2. Codification in Compressive Spectral Imaging

Compressive sensing (CS) is known to be a convenient tool when a large amount of data is required to be processed in a particular application, when there is a limitation of time or storage of the data, or when the complete sampling of a scene is unfeasible. An area where CS is of great interest is the spectral imaging, since the data acquired and processed increases exponentially when additional spectral bands are required, generating the development of many compressive spectral imaging (CSI) systems [13, 35, 36] such as the multi-aperture filtered camera (MAFC), the coded aperture snapshot spectral imager (CASSI) [37], and the snapshot hyperspectral imaging Fourier transform (SHIFT). CSI senses and compresses the spatio-spectral information simultaneously in the form of two-dimensional(2D) projections at the detector. These systems are modulation-based, requiring an optical element known as coded aperture, and are usually referred to as optical coding systems. The main components of optical coding systems are focal plane arrays (FPA), spatial light modulators (SLM), modulation devices such as digital micromirror devices (DMD) or photomasks, and dispersive elements [8, 35]. The modulation of the spatial-spectral field through a coded aperture (CA) and the multiplexing using a dispersive element are the fundamental operations allowing the sensing of 2D projections. The CA is important in these systems since it is the sole element we can directly modify.

The CA is modeled as an array where each spatial coordinate has a particular response to the incoming wavefront. Depending on the nature of the entry values, there are polarizer CA [38], complex-modulating CA [39], phase CA [40], intensity-modulating CA [41], among others. The implementation of intensity-modulating CA can be realized through a photomask with a permeability to block or unblock the light in wide or narrow spectral band ranges, with DMDs, or more recently with diffractive optical elements (DOE). Advances in CSI include the CA designs, the use of different devices for the implementation of those patterns, and their applications [21,42].

2.1. Coded Aperture

A 2D coded aperture defined as $\mathbf{T}$ could have binary, real, or complex entries depending on the nature of the field. In the most general case, given its implementation simplicity, the CA has binary entries such that $t_{i,j} \in \{0,1\}$. Assuming that the light response remains approximately constant over a spatial square region of size $\Delta_p \times \Delta_p$ in the CA, and have a specific response to the incoming light, the transmittance function of the coded aperture is given by

$$\mathbf{T}(x,y) = \sum_{m,n} t_{m,n} \mathrm{rect}\left(\frac{x}{\Delta_p} - m, \frac{y}{\Delta_p} - n\right), \tag{1}$$

where (x,y) are the spatial coordinates of the observed scene and (m,n) are the CA pixel coordinates.

Moreover, a 3D coded aperture models the 2D spatial distribution projected on a third dimension, depending on the study field. Particularly, in CSI, the spectrum can be modulated through optical filters located at each spatial location of the 2D CA by means of a colored-CA. A polarizer-CA modulates the scene using micro-polarizer arrays with different angles. For video applications, the temporal-CA modulates spatially or spectrally the frames along the time [33]. In the case of the depth-CA, the modulation is realized to the depth and angular views. The transmittance in the case of a 3D CA is defined as,

$$\mathbf{T}(x,y,\lambda) = \sum_{m,n} t_{m,n,\ell} \mathrm{rect}\left(\frac{x}{\Delta_p} - m, \frac{y}{\Delta_p} - n, \frac{\lambda}{\Delta_\lambda} - \ell, \right), \tag{2}$$

where the modulation is performed over the third dimension. In the case of CSI, the third dimension is the spectrum λ, i.e., this is the mathematical representation of the colored-CA. Figure 1 shows different 2D and 3D CA representations.

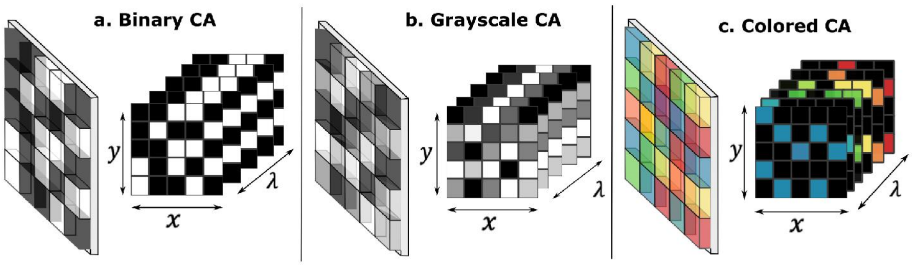

Fig. 1. Spectral-based coded apertures physical and mathematical representations. (a.) A binary CA with $0,1$ entries. (b.) A grayscale CA with $[0,1]$ entries. (c.) A colored-CA with specific wavefront responses.

2.2. Forward Model in Compressive Spectral Imaging Systems

In a general form, the forward model in CSI systems is defined by the mathematical projections acquired using coded apertures as the modulation device over a scene $\mathcal{F}_{ijk}$, where $i \in \{1.,\ldots,N\}$ and $j \in \{1.,\ldots,N\}$ index the spatial coordinates, and $k \in \{1.,\ldots,L\}$ determines the k^{th} spectral plane. The model is given by,

$$\tilde{\mathbf{g}} = \tilde{\mathbf{H}}\tilde{\mathbf{f}} + \tilde{\boldsymbol{\omega}}, \tag{3}$$

where $\tilde{\mathbf{g}} \in \mathbb{R}^m$ are the measurements or 2D encoded projections, $\tilde{\mathbf{H}} \in \mathbb{R}^{m\times n}$ models the sensing matrix, $\mathbf{f}$ is the vector representation of the spectral signal, and $\tilde{\boldsymbol{\omega}}$ is the white noise of the sensing system. The modeling of $\tilde{\mathbf{H}}$ is determined by the optical coding system and the operations involved in their respective configuration, such as the modulation by the corresponding CA. In the case of spectral imaging systems, a required device to multiplex the spectral information is a dispersive element such as a prism or a diffractive element. In this case, the matrix $\tilde{\mathbf{H}}$ is defined depending on the architecture as $\tilde{\mathbf{H}} = \mathbf{PT}$, for instance, for the CASSI system, where $\mathbf{P}$ represents the dispersive function of the prism and $\mathbf{T}$ is determined by the coded aperture. Depending on the application, several projections can be required. For S snapshots, each measurement $\tilde{\mathbf{g}}^S$ is obtained with a different coded aperture $\mathbf{T}^S$, and therefore a different sensing matrix $\tilde{\mathbf{H}}^S$. The multishot acquisition process can be succinctly defined as

$$\mathbf{g} = \mathbf{H}\mathbf{f} + \boldsymbol{\omega}, \tag{4}$$

where the set of S snapshots in Eq. 4 can be assembled into a single vector by concatenating the $\tilde{\mathbf{g}}^S$ vectors in order to create the overall measurement vector denoted as $\mathbf{g} = [(\tilde{\mathbf{g}}^1)^\intercal, \ldots, (\tilde{\mathbf{g}}^S)^\intercal]^\intercal$, where $\mathbf{H} = [(\tilde{\mathbf{H}}^1)^\intercal, \ldots, (\tilde{\mathbf{H}}^S)^\intercal]^\intercal$, and $\boldsymbol{\omega} = [(\tilde{\boldsymbol{\omega}}^1)^\intercal, \ldots, (\tilde{\boldsymbol{\omega}}^S)^\intercal]^\intercal$. The compression ratio depends directly on the number of shots acquired, using the relation $\gamma = Sm/n$.

2.3. Compressive Spectral Imaging Systems

In a general form, the use of different systems is translated in the definition of the **H** transfer function. This matrix is composed of diagonals corresponding to the coded aperture patterns applied to each waveband, in the case of CSI systems. Additionally, the dispersion operation resulting from the dispersive elements is modeled by the shifting of those diagonals. Figure 2 shows different CSI implementations for real spectral acquisitions. The dual disperser (DD-CASSI) architecture encodes spectral content for each spatial position through two dispersive elements and one CA [43]. The single disperser (SD-CASSI), one of the most popular imaging systems in literature, since reduces the calibration complexity compared with the DD-CASSI uses one CA located at the image plane and a single prism or grating before the detector [37]. As a result, spatio-spectral coded projections are measured using this architecture. The colored coded aperture imager (3D-CASSI) extends the DD-CASSI and the SD-CASSI modulation by the inclusion of spectral filters, which encode also the spectral information [44]. The advances on the CSI arquitecture designs expand the capabilities of the spectral information since, they allow to reconstruct higher quality spectral information and troublesome scenes, but also bring complexity issues, they require additional optical elements, the sensitivity to calibration errors increases, and the light throughput diminishes. A recent multishot CSI system proposed to overcome some of the drawbacks mentioned before is based on the use of deformable mirrors (DM-CASSI), which provides dynamic phase modulation capabilities and enables multiframe coding with a low loss of radiant energy flow [45]. A sketch of the respective optical setups of the CSI systems mentioned before and the **H** transfer function is shown in figure 2. The location of the coded apertures in the optical path determines the structure of the transfer function, as can be seen in the presented acquisition matrices. The conditionally of the measurement matrix depends on the transfer function of the system, consequently, the complexity of the reconstruction. The acquisition of three shots is reflected in the composition of the **H** matrix, shown in the bottom part of the figure.

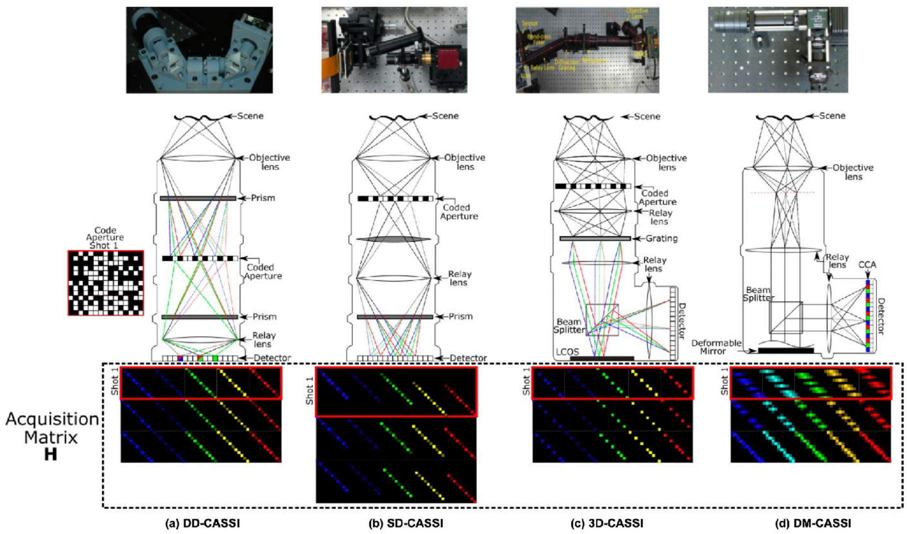

Fig. 2. Multishot compressive spectral cameras. (a) DD-CASSI, (b) SD-CASSI, (c) 3D-CASSI, and (d) DM-CASSI.

2.4. Reconstruction algorithms

Most of the CASSI-related systems rely on CS sparse reconstruction algorithms to recover the data cube by exploiting spatio-spectral redundancies in a transform domain. An estimation of the spatio-spectral data cube can be attained by solving the regularization problem,

$$\hat{\mathbf{f}} = \mathbf{\Psi}\{\text{argmin}_{\theta}\|\mathbf{g} - \mathbf{H}\mathbf{\Psi}\boldsymbol{\theta}\|_2 + \tau\|\boldsymbol{\theta}\|_1\}, \tag{5}$$

which assumes that $\mathbf{f} = \mathbf{\Psi}\boldsymbol{\theta}$, meaning $\boldsymbol{\theta}$ represents an S-sparse representation of $\mathbf{f}$, and τ is a regularization constant. The basis representation $\mathbf{\Psi}$ sparsifies the image, and it can be Wavelet, DCT, a Kroneckcer product of them, or a dictionary specifically designed for the data. The first term in Eq. 5 minimizes the Euclidean distance between the measurements and the contribution from the estimate $\boldsymbol{\theta}$, while the second term promotes sparsity of the reconstruction.

Different algorithms have been proposed to solve the optimization problem in Eq. 5, including the two-step iterative shrinkage/thresholding (TwIST) [15], the gradient projection for sparse reconstruction (GPSR) [16], Gaussian mixture models (GMM) [17], the compressive imaging reconstruction algorithm based on the approximate message passing (AMP) framework [18], or more recently deep learning-based reconstruction algorithms such as the hyperspectral image reconstruction using a deep spatial-Spectral prior (HIR-DSPP) [19], and the HyperReconNet [20].

3. Coded Aperture Optimization

A system using the modulation through coded apertures is usually implemented to perform a specific task. Among them, the reconstruction [22–30] is the most general application since it is the basis for other high-level applications such as classification [31], clustering [32], and fusion [34] of spectral images. The optimization of the coded aperture pattern is a widely studied topic since state-of-the-art works have shown the structure of the patterns determines the achieved quality. Four different methods can be identified to design CA in order to achieve higher quality results, reduce even more the required number of measurements, or both at the same time. The first method relies on the spatial structure of the pattern; a second method consists of mathematical optimization of the sensing matrix $\mathbf{H}$. The third mathematical optimization includes in the optimization problem, the representation basis, such that the optimization is performed over $\mathbf{H\Psi}$. A fourth and more recent approach is a data-dependent solution based on deep learning. Figure 3 lists the multi-shot coded aperture design approaches reported in this paper. As can be noticed, they can be sub-divided into data-independent and data-dependent methods. The complexity of the optimization problem increases from one method to the other in the order they are listed. Since the design aims to generate a coded aperture or the set of codes for the acquisition, the approaches operate directly over $\mathbf{T}$ or indirectly over the sensing matrix $\mathbf{H}$, as shown in the diagram.

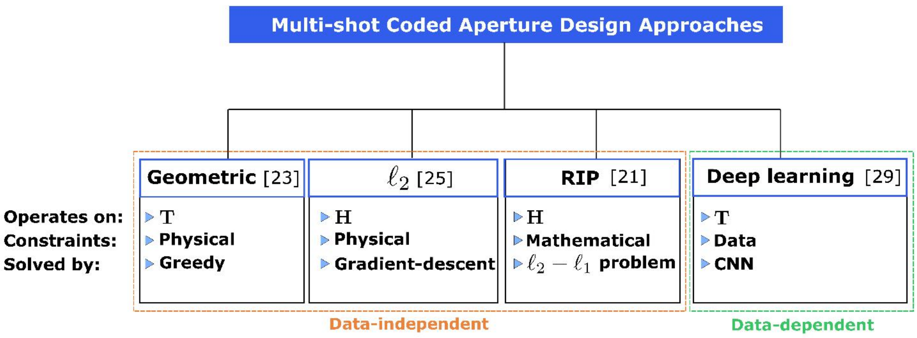

Fig. 3. Coded aperture design approaches. The dependence on data also divides the approaches for the CA design.

3.1. Geometrical optimization

The geometrical optimization method modifies the spatial entries of $\mathbf{T}$, analyzing the locations of the one-values and zero-values and exchanging the required entries to produce more uniform patterns [24]. Five conditions are evaluated through Greedy algorithms; four of them are grouped in an intra-shot condition, which seeks to maximize the horizontal, vertical, and diagonal separations between the one-valued entries of $\mathbf{T}$, which in essence, requires the codes to satisfy spatial blue noise pixel distribution. The two conditions regarding the entries in the diagonals help to reduce the cluster occurrences. The fifth condition, termed inter-shot, aims to reduce the correlation across shots, which is equivalent to having just one coded aperture pixel set to one at each particular spatial position of the CA ensemble. A weighted penalization is allowed with the definition of a weighted local metric,

$$G_p = \sum_{p=1}^{5} w_p ||d_p||_1, \tag{6}$$

where w_p corresponds to the weights specified to each of the five conditions, and d is the evaluation of the amount of one-valued entries given the condition p. An optimal CA ensemble can be obtained by minimizing the variance of G_p, given that all the S CA in the ensemble are intended to exhibit the same transmittance. This is achieved by solving the optimization problem

$$\underset{\{\mathbf{T}^1,\ldots,\mathbf{T}^K\}}{\arg\min} \ var(G_p) \quad \text{subject to} \sum_{i=1}^{S} \mathbf{T}^i = 1. \tag{7}$$

A greedy algorithm calculates the concentration of one-valued entries $||d_p||$, which are then used to calculate G_p. The coded aperture with the minimum concentration of ones calculated in Eq. 7 is the one finally chosen. Figure 4 presents a graphic representation of the geometrical approach. The intra-shot and the inter-shot conditions are shown for a reduced version of a CA. The designed CA ensemble, as well as its colored representation, are also presented.

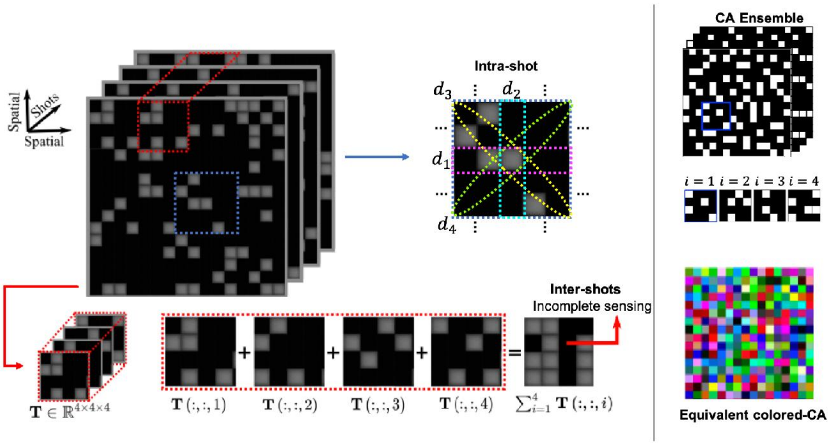

Fig. 4. Geometrical optimization of spatial one-valued entries of a CA $\mathbf{T}$. The resulting CA ensemble of 4 shots is presented together with the equivalent colored-CA.

3.2. ℓ_2 optimization

A more theoretical approach designs the distribution of the binary coding elements in a structured, sparse, and binary measurement matrix [26]. This condition is satisfied by minimizing the number of zero eigenvalues of the matrices $\mathbf{G} = \mathbf{H}^\intercal\mathbf{H}$ and $\hat{\mathbf{G}} = \mathbf{H}\mathbf{H}^\intercal$, which is translated in increasing the number of lineal independent rows and columns of the measurement matrix [27]. Equivalently, this leads to maximizing the rank of $\mathbf{H}$ and having a better-conditioned matrix, and therefore a better sensing matrix. To formulate the respective optimization problem, $(\mathbf{q})_i$ and $(\mathbf{p})_j$ are defined as the sum per row or the number of signal elements measured by the detector, and the sum per column or the number of times a particular signal element is measured, respectively,

$$(\mathbf{p})_i = \sum_{j=1}^{m} \mathbf{H}_{i,j} = \mathbf{1}_M^\intercal \mathbf{H}, \qquad (\mathbf{q})_i = \sum_{j=1}^{n} \mathbf{H}_{i,j} = \mathbf{H}\mathbf{1}_N, \tag{8}$$

where $\mathbf{1}_N$ is defined as an $N-$long vector of ones. Then, the optimization problem to solve, in order to achieve an uniform sensing is,

$$\underset{\mathbf{p},\mathbf{q}}{\arg\min} \, ||\mathbf{p} - (U/N)\mathbf{1}_N||_2^2 + ||\mathbf{q} - (U/M)\mathbf{1}_M||_2^2, \tag{9}$$

where U/N and U/M are the expected one-entry values per row and column, and U is a constant referring to the total number of non-zero elements. In terms of $\mathbf{H}$, Eq. 9 can be expressed as,

$$\underset{\mathbf{H}}{\arg\min} \, ||\mathbf{1}_M^\intercal \mathbf{H} - (U/N)\mathbf{1}_N^\intercal||_2^2 + ||\mathbf{H}\mathbf{1}_N - (U/M)\mathbf{1}_M||_2^2, \tag{10}$$

$$\text{subject to}[\mathbf{H}]_{i,j} = 0 \quad \forall (i,j) \in \Omega^C,$$

where Ω is the set of ordered pairs containing the non-zero entries of the measurement matrix, which restricts the modifiable positions of $\mathbf{H}$ obtained by specifying the hardware setting and Ω^C is its complement. The previous problem is solved through a gradient descent approach that minimizes the associated objective function by optimal selection of the non-zero elements per row and column. Figure 5 depicts the intuition behind this method; the uniform sum per row and per column values in the acquisition matrix $\mathbf{H}$. A designed colored-CA using this approach is also included in the figure.

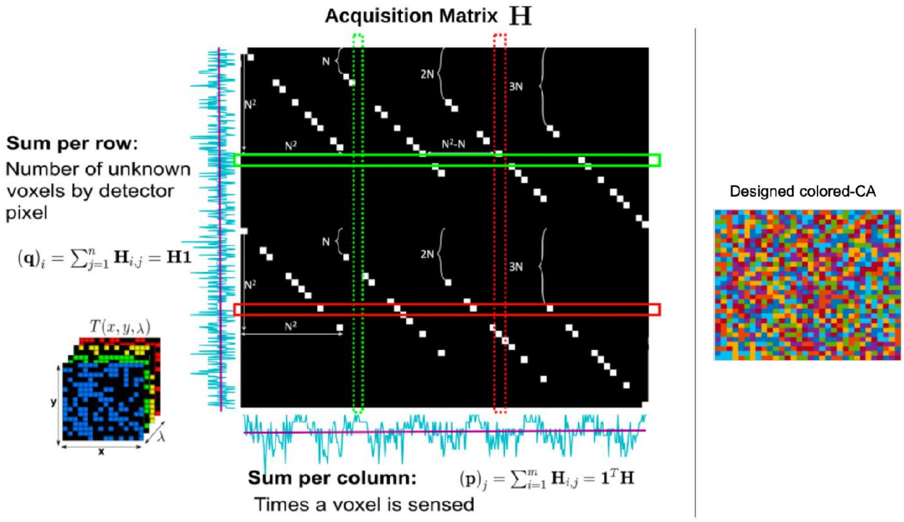

Fig. 5. ℓ_2 mathematical optimization of acquisition matrix $\mathbf{H}$. The sums per row and per column are the base of this method.

3.3. Restricted Isometry Property optimization

The most complex approach from the data-independent methods is based on the Restricted Isometry Property (RIP) [22]. The RIP of the matrix $\mathbf{A} = \mathbf{H}\boldsymbol{\Psi}$ is critical in the design of the CA since it guarantees the probability of correct reconstruction. The RIP optimization involves the transformation basis of the data, such that $\mathbf{f} = \boldsymbol{\Psi}\boldsymbol{\theta}$ and $|\boldsymbol{\theta}| = R$. The RIP is then defined as the smallest δ_R, such that,

$$(1-\delta_R)\|\boldsymbol{\theta}\|_2^2 \leq \|\mathbf{A}\boldsymbol{\theta}\|_2^2 (1+\delta_R)\|\boldsymbol{\theta}\|_2^2. \tag{11}$$

The constant δ_R can be calculated as

$$\delta_R = \max_{|\mathcal{T}|\leq R} \lambda_{max}(\mathbf{A}_{\mathcal{T}}^{\intercal}\mathbf{A}_{\mathcal{T}} - \mathbf{I}), \tag{12}$$

where $\lambda_{max}(\cdot)$ denotes the largest eigenvalue and $\mathbf{I}$ is an identity matrix. Given that the sensing matrix $\mathbf{A}$ is determined by the matrix $\mathbf{H}$ and the basis representation matrix $\boldsymbol{\Psi}$; the entries of the sub-matrices $\mathbf{A}_{\mathcal{T}}$, containing $\mathcal{T}$ arbitrary columns of $\mathbf{A}$ indexed by $\mathcal{T} \subset [N^2L]$ can be expressed as the product of the basis representations columns $[\psi_0, \ldots, \psi_{N^2L-1}]$ and the $\mathbf{h}_i$ columns. Then, $(\mathbf{A}_{\mathcal{T}})_{ir} = \mathbf{h}_i\psi_{\Omega_r} = \sum_{k=0}^{L-1}(\mathbf{t}_k^{S_i})_{m_i-kN}\psi_{m_i+k(N'),\Omega_r}$, with $i = 0,\ldots,SV-1$, $r = 0,\ldots,\mathcal{T}-1$, $S_i = \lfloor i/V \rfloor$, $S_i \in \{0,\ldots,S-1\}$, $m_i = i - S_iV$, $N' = N^2 - N$, $\Omega_r \in \{0,\ldots,N^2L-1\}$, and $V = N(N+L-1)$.

A normalization of the correlation matrix $(\mathbf{A}_{\mathcal{T}}^{\intercal}\mathbf{A}_{\mathcal{T}})'$ is performed to guarantee the calculation of the λ_{max}. Based on the RIP for sub-Gaussian random ensembles in [46], this design method models the entries of the correlation matrix as sub-Gaussian random variables with the aim to use them to determine the RIP constants. Accordingly, each element of the normalized matrix $(\mathbf{A}_{\mathcal{T}}^{\intercal}\mathbf{A}_{\mathcal{T}})'_{r,u}$ for $r,u = 0,\ldots,|\mathcal{T}|-1$ is the sum of bounded random variables, which can be expressed as

$$(\mathbf{A}_{\mathcal{T}}^{\intercal}\mathbf{A}_{\mathcal{T}})'_{r,u} = \sum_{s=0}^{S-1}\sum_{i=0}^{V-1}\sum_{k_1=0}^{L-1}\sum_{k_2=0}^{L-1}(\mathbf{t}_{k_1}^s)_{i-k_1N}(\mathbf{t}_{k_2}^s)_{i-k_2N}\Psi_{i+k_1N',\Omega_r}\Psi_{i+k_2N',\Omega_u}/C, \tag{13}$$

where $\Omega_u \in \{0,\ldots,N^2L-1\}$, and C is a constant resulting from the normalization over the correlation matrix. From Eq. 13, some auxiliary terms are defined, $\Pi_{xyz} = \sum_{s=0}^{S-1}(\mathbf{t}_x^s)_y(\mathbf{t}_{x-z}^s)_{y+zN}$, $\phi_{xy}^{ru} = \Psi_x^{2D}\Psi_y^{2D}$, and $\mathcal{W}_{xy}^{ru} =$

$\mathbf{W}_{x-y,\Gamma_u}\mathbf{W}_{x\Gamma_r}u[-y]+\mathbf{W}_{x,\Gamma_u}\mathbf{W}_{x-y\Gamma_r}u[y-1]$ where $\Gamma_x = \lfloor \Omega_x/N^2 \rfloor$, and $u[x]$ is the step function of x. These auxiliary terms are used to define the variable

$$\beta_{jru} = \sum_{k_2=0}^{L-1-|q_j|} \Pi_{k_2,p_j,q_j} \mathcal{W}^{ru}_{k_2,u_j}/C. \tag{14}$$

Finally, the entries $(\mathbf{A}_{\mathcal{T}}^{\intercal}\mathbf{A}_{\mathcal{T}})'_{r,u}$ can be expressed as

$$(\mathbf{A}_{\mathcal{T}}^{\intercal}\mathbf{A}_{\mathcal{T}})'_{r,u} = \sum_{j=0}^{N_L} \phi^{ru}_{p_j,q_j}\beta_{jru}/C, \tag{15}$$

for $N_L = N^2(2L-1)-1$, $p_j = \lfloor j/(2L-1) \rfloor$, and $q_j = j - p_j(2L-1)-(L-1)$. The detailed procedure can be found in [22] and [24], where it is assumed that variables in Eq. 15 are bounded such that $|\phi^{ru}_{p_j,q_j}| < B$. Since the entries of the correlation matrix are modeled as a sub-Gaussian random variables, then $(\mathbf{A}_{\mathcal{T}}^{\intercal}\mathbf{A}_{\mathcal{T}})'_{r,u} \sim Sub(\nu^2)$. Therefore, the probability of correct reconstruction can be maximized by minimizing the sub-Gaussian constant ν defined as,

$$\nu = \max_{r,u} B \sum_{j=0}^{N_L} \beta_{jru}, \tag{16}$$

or equivalently by properly designing the coded aperture ensembles. Particularly, the optimization problem resulting from this method was solved via a Genetic algorithm. The parameters and more detailed information is reported in [22]. Figure 6 shows a representation of the analysis performed over $\mathbf{A}$ and, more specifically, over the sub-matrices $\mathbf{A}_{\mathcal{T}}$. Notice the inclusion of the representation basis in the analysis. A resulting designed colored-CA is also depicted in the figure.

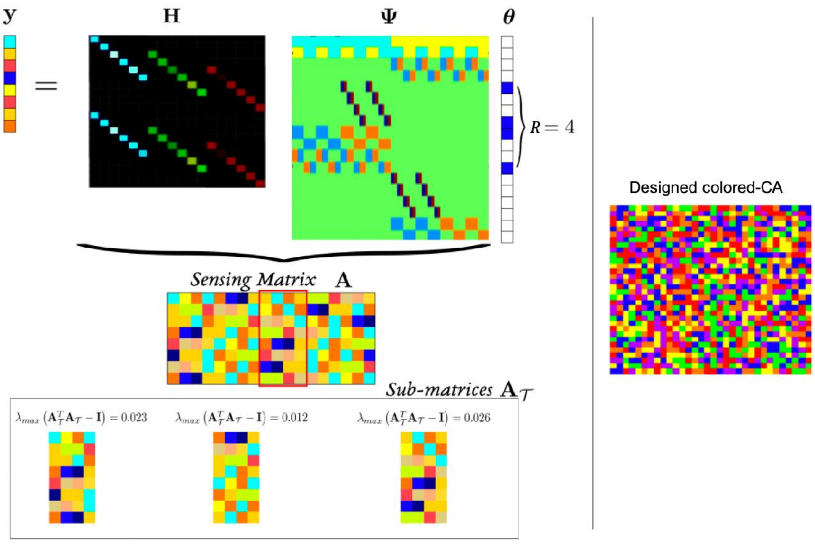

Fig. 6. RIP mathematical optimization for the coded aperture design. The transformation basis of the data is included in the optimizations. The submatrices $\mathbf{A}_{\mathcal{T}}$ are the basis of this optimization approach.

3.4. Deep learning optimization

This approach nowadays aims to design the sensing matrix together with an inference network under an end-to-end (E2E) optimization [30,47,48]. A cost function with two terms is solved; the first term related to the task is the loss function $\mathcal{L}_{task}(\cdot,\cdot)$, and a customizable regularization function $R(\mathbf{T})$ promotes particular properties in the expected CAs. Since this method is data-dependent, several scenes $\mathbf{f}_k$, as well as their corresponding task outputs $\mathbf{d}_k$, for a number of $k = 1,\ldots,K$ scenes are required for this optimization. The coupled optimization problem is formulated as

$$\mathcal{L}(\mathbf{T},\theta|\mathbf{f},\mathbf{d}) = \frac{1}{K}\sum_k \mathcal{L}_{task}(\mathcal{M}_\theta(\mathbf{H_T}\mathbf{f}_k),\mathbf{d}_k) + \rho R(\mathbf{T}), \tag{17}$$

where $\mathbf{H_T}$ is the sensing matrix, with the set of CAs $\mathbf{T}$, θ are the parameters of a deep neural network (DNN) $\mathcal{M}_\theta(\cdot)$, and $\rho > 0$ is a regularization parameter.

Figure 7 presents an overview of the approach. Two main parts are differentiable, training and testing part. In the first part, an optical layer is connected to a task module. The sensing matrix $\mathbf{H_T}$, and the DNN parameters are learned in the training step. Once the set of CAs is optimized for the specific task, real measurements $\bar{\mathbf{g}}$ can be acquired using the learned CAs, meaning the optical layer is replaced by a physical optical layer, and the pre-trained DNN or inference operator is applied to estimate the task output $\bar{\mathbf{d}} = \mathcal{M}_{\theta^*}(\bar{\mathbf{g}})$.

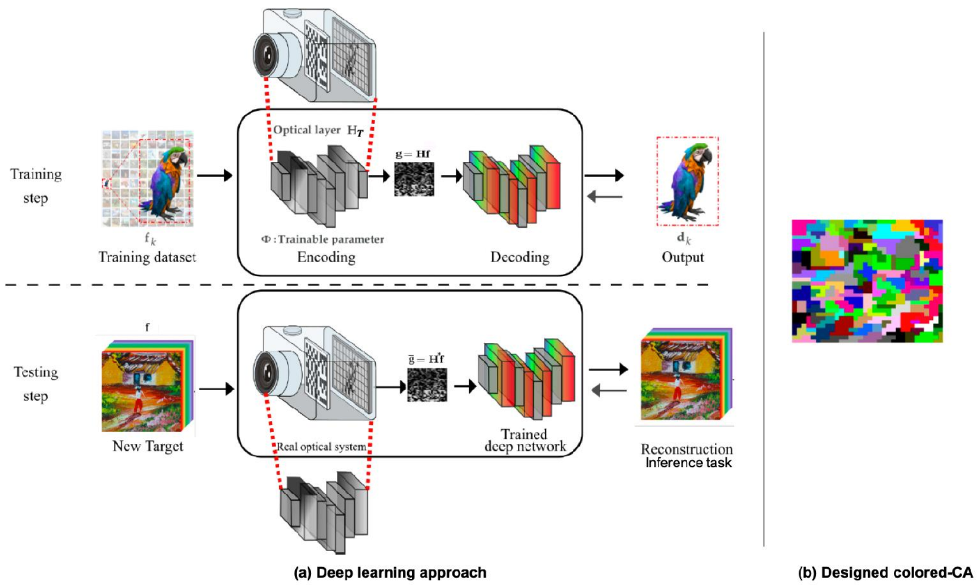

Fig. 7. Deep learning approach for coded aperture design. The CA optimization and the task-specific neural network are learned and then used in a real setup to achieve high-quality spectral imaging results. An example of the generated colored-CA is presented.

4. Deep learning regularization for CA design improvement

Deep learning methods have shown great capabilities in the last years in the computational imaging area. Extending the potentiality of the technique, the inclusion of customizable regularization helps not only improve the performance achieved as in Eq. 17 but to promote particular properties in the designed CA. These properties are related mainly to the optical implementation of those CA. Different regularizations have been studied [30] such as the implementability, transmittance, number and correlation between snapshots, and conditionality constraints. These regularizations are designed using a family of functions with specific behavior. Some of them are listed below.

An implementability regularization to constraint the entries of the CA can be used to restrict the values to either (0) or (1), to (-1) or (1), or real values $\mathbf{T} \in [0,1]$, which extends the binary cases. The first mentioned regularizer, for instance, is defined as,

$$R(\mathbf{T}) = \frac{1}{S}\sum_{S}\sum_{i,j,\ell}((\mathbf{T}^S_{i,j,\ell})^2)^{p_1}(\mathbf{T}^s_{i,j,\ell}-1)^2)^{p_2}, \tag{18}$$

where S is the number of snapshots and $p_1, p_2 \in \mathcal{R}_{[++]}$ are two hyper-parameters providing variability in the family of functions curve addressing this binary constraint.

Another important constraint directly related to the implementation is the CA transmittance level. In spectral imaging, higher transmittance levels are desired since it increases the signal-to-noise power ratio; in contrast, in X-ray tomography, lower transmittance levels are desired since these minimize the scene radiation. The following regularization function regulates the expected transmittance with the performance of the system

$$R(\mathbf{T}) = \frac{1}{S}\sum_{S}\left(\frac{\sum_{i,j,\ell}\mathbf{T}^S_{i,j,\ell}}{MNL} - \gamma\right)^2, \tag{19}$$

where $\gamma \in [0,1]$ is the range of possible values of transmittance. In addition to the presented implementation or assembling constraints, others can be defined with the aim to improve the performance of the inference task intended to solve. For instance, the correlation between shots in a multishot scheme can be reduced by using a generalized function that minimizes the correlation between the S CAs.

$$R(\mathbf{T}) = \frac{\sum_{i,j,\ell}(\prod_S \mathbf{T}^S_{i,j,\ell})}{MNL}. \tag{20}$$

Fig. 8. Reconstructions using the designed coded apertures through the five methods reported. (a) Ground truth scene. Reconstructed scene using (b) random CA, (c) Geometric CA, (d) ℓ_2 CA, (e) RIP CA, and (f) Deep learning CA.

5. Application of Coded Aperture Optimization

The coded aperture optimization has been widely studied for different applications. The common performance comparison is conducted with a baseline coded aperture or previous CA designs showing high-quality outputs. Since random matrices are largely incoherent with any fixed basis $\mathbf{\Phi}$, randomness is a very effective sensing mechanism. Sensing matrices exhibiting such randomness can be generated using random CAs. In fact, it has been shown that the random measurement matrices are universal, e.g., there is no need to know the sparsity basis transformation when designing the measurement system [46,49]. For these reasons, random CAs are the baseline CA used for comparison purposes.

The reconstruction of spectral images is not only one primary application in computational imaging; it is the starting point of other high-level tasks such as detection, classification, and fusion unless the inference is developed without previous reconstruction. For that reason, it can be used as an example of the behavior of the different CA design techniques.

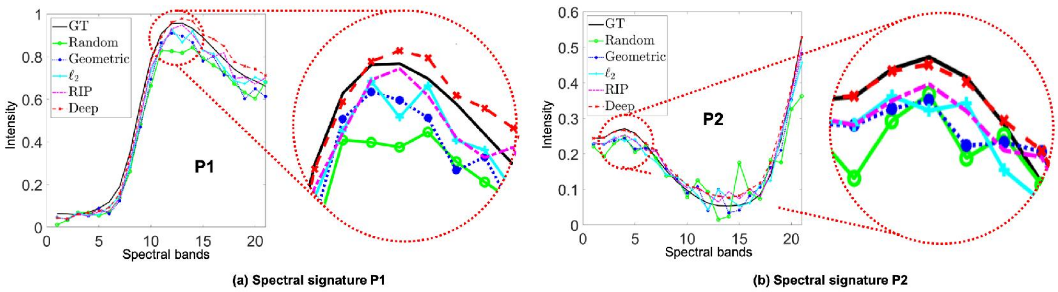

Fig. 9. Reconstructed spectral signatures at two representative spatial points indicated as P1 and P2 in ground truth image in Fig. 8. The black curve is the ground truth spectral signature, and the other five curves are the reconstructed profiles obtained with each of the methods.

Figure 8 shows a real spectral scene used to simulate the acquisition and reconstruction under the compressive sensing paradigm using the state-of-the-art SD-CASSI optical coding system. The same simulations can be performed using other spectral systems; since the SD-CASSI implementation is less complex than other architectures, it was chosen for the simulations, despite the challenge of spatial information reconstruction inherent with this system given the dispersion operation induced by the prism. Since the goal with the experiments is the CA designs comparison, the same reconstruction method is used, and there is no detailed analysis in the reconstruction

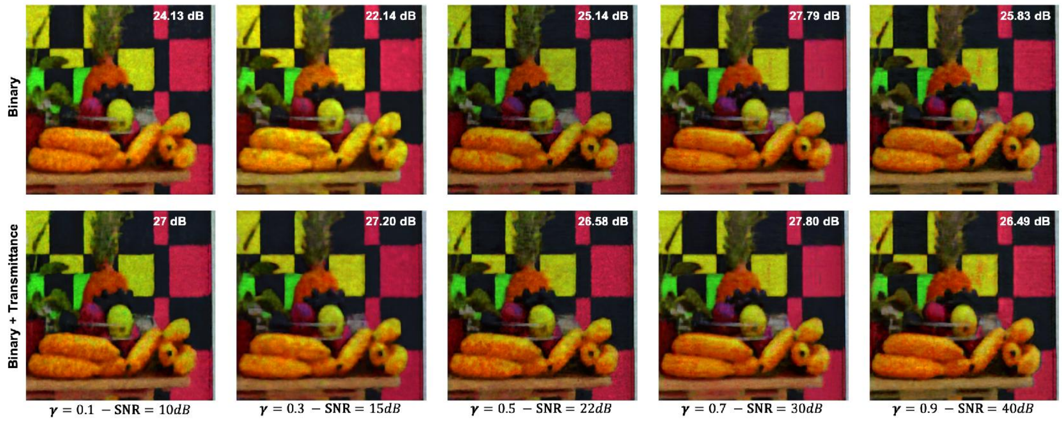

Fig. 10. Spatial reconstructions using deep learning designed CA with two different configurations. First row reconstructions were obtained including the binary regularizations in Eq. 18. Second row reports reconstructions using a combination of the binary (Eq. 18) and the transmittance (Eq. 18 and Eq. 19) regularization.

method. In this case, the scene was reconstructed using a data-driven recovery network from literature, the HyperReconNet [20], using the same hyper-parameter tuning process. Figure 8 reports an RGB visual representation comparison of the spatial quality achieved using the different CA design strategies. For numerical comparison, the mean spectral peak SNR (PSNR) is also reported for each reconstruction. The improvement in the visual results increases with the CA design approach complexity. The spectral quality is also presented in Fig. 9 for two points referred to as P1 and P2 in the ground truth scene in Fig. 8. The zoomed sections show how far the reconstructed spectral signatures are from the black curve, which is the ground truth (GT) profile. The same behavior observed in the spatial reconstructions is also presented in the recovered spectral signatures. Notice that all the designed CA outperforms the baseline, which is the random CA. From the data-independent methods, the CA designed using the RIP is the one achieving the higher quality. On the other hand, the deep learning method produces the best CA designs from the compared methods. To compare the computational complexity of the four methods is important to mention that the running time for the RIP and deep learning methods is considerably higher compared with the other approaches, the RIP optimization is in the order of days and the deep learning in the order of weeks; in the case of the RIP, because of the size of the matrix $\mathbf{A}$ and in the case of the deep learning, because it requires the training step; the other methods run in the order of minutes.

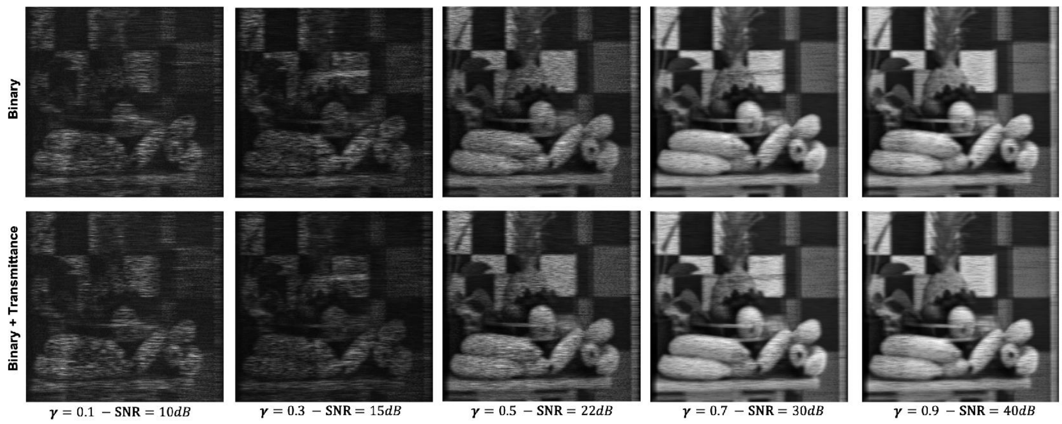

Fig. 11. The measurements using the same configurations reported in Fig. 10 for two cases. First row: Using binary regularization (Eq. 18). Second row: Using binary and transmittance (Eq. 18 and Eq. 19) regularization.

The performance of the CA resulting from the deep learning optimization motivates to find strategies to design CA, which not only guarantee the corresponding task achievement but promote at the same time implementability capabilities. The regularizers defined in Eqs. 18, 19, and 20 are used to demonstrate for the same previous reconstruction task, different design configurations. In Fig. 10 the reconstructions obtained using the binarization regularizer in Eq. 18 and a combination of binarization and transmittance regularizers in Eq. 18 and 19 are depicted. In each case, five different configurations are tested, varying the γ parameter in Eq. 19 from 0.1 to 0.9. As can be noticed, the transmittance affects the SNR since the light incoming in the detector is modified with this parameter. The PSNR metric is also included for each configuration, showing a trade-off between transmittance and reconstruction quality. The corresponding measurements for each configuration are shown in Fig. 11. The transmittance level is noticeable in all the configuration cases. It is important to highlight that all the measurements were acquired under the same light conditions.

On the other hand, the application of the same two cases of the previous experiment and a third case, which uses the shot correlation regularizer en Eq. 20 is reported in Fig. 12. In this experiment, the reconstructions are obtained using 6 and 7 shots. The quality comparison plot shows clearly that the use of the 3 regularizers together results in the same performance achieved with only the binarization regularizer but acquiring 7 shots, which demonstrates the capabilities of the regularizers.

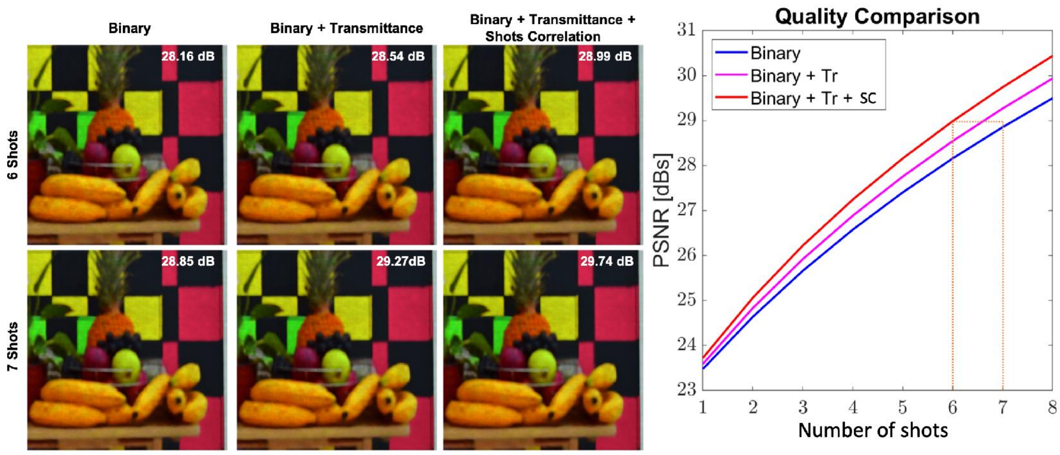

Fig. 12. Spatial reconstruction quality using combinations of regularizers in the deep learning approach and acquiring 6 and 7 shots.

6. Conclusions

This review paper presented research advances in optical codification design in compressive spectral imaging. Understanding the contribution of the coded apertures in optical architectures under the compressive sensing paradigm allowed progress in the area. Four different methods for designing coded apertures have been proposed to improve the final quality of reconstructed spectral images. These methods are divided into two main categories, data-independent and data-dependent approaches, which determine the complexity in terms of data requirements, which is higher for the deep learning (data-dependent) optimization. The reconstruction quality also reflects the performance of the methods. The reconstruction results show the improvement is remarkable for the deep learning and the RIP methods. However, contrary to the reconstruction quality conclusions, the computational cost expressed in running time is higher for the methods yielding the higher quality, i.e., the deep-learning and RIP approaches; they require weeks and days of offline computations, respectively.

It is important to emphasize that the coded aperture design approaches reported can be extended to several compressive architectures, such as spectral imaging sensors [50], seismic data acquisition [51] [52], and phase retrieval imaging [53]. All the proposed methods overcome the random coding, which is the baseline for comparisons.

Acknowledgments

This work was supported by the project 110287780575 through the agrement 785-2019 between the *Agencia Nacional de Hidrocarburos*, the *Ministerio de Ciencia, Tecnología e Innovación* and the *Fondo Nacional de Financiamiento para la Ciencia, la Tecnología y la Innovación Francisco José de Caldas*. Laura Galvis was supported by the postdoctoral research program of the VIE-UIS.

